JOURNAL OF SPACECRAFT AND ROCKETS
Vol. 38, No. 5, September–October 2001

Assessment of One- and Two-Equation Turbulence Models for Hypersonic Transitional Flows

Christopher J. Roy* and Frederick G. Blottner†
Sandia National Laboratories, Albuquerque, New Mexico 87185

One- and two-equation turbulence models are examined for hypersonic perfect- and real-gas flows with laminar, transitional, and turbulent flow regions. These models were generally developed for incompressible flows, and the extension to the hypersonic flow regime is discussed. In particular, the compressible formulation of the turbulence diffusion term for one-equation models is examined. For the Spalart–Allmaras model, the standard method for forcing transition at a specified location is found to be inadequate for hypersonic flows. An alternative transition method is proposed and evaluated for a Mach 8 flat plate test case. This test case is also used to evaluate three different two-equation turbulence models: a low-Reynolds-number k–ε model, the Menter k–ω formulation, and the Wilcox k–ω model. These one- and two-equation models are then applied to the Mach 20 Reentry F flight vehicle. The Spalart–Allmaras model and both k–ω formulations are found to provide reasonable agreement with the flight data for heat flux, whereas the Baldwin–Barth and low-Reynolds-number k–ε models overpredict the turbulent heating rates by a factor of two. Careful attention is given to the numerical accuracy of the solutions in the areas of both iterative and grid convergence.

Nomenclature

a = speed of sound, m/s
c_{b1} = turbulence modeling constant, 0.1355
c_{b2} = turbulence modeling constant, 0.622
c_{t1} = transition modeling constant, 1.0
c_{t2} = transition modeling constant, 2.0
c_{t3} = transition modeling constant, 1.2
c_{t4} = transition modeling constant, 0.5
c_{v1} = turbulence modeling constant, 7.1
c_{w1} = turbulence modeling constant, 3.24
c_{w2} = turbulence modeling constant, 0.3
c_{w3} = turbulence modeling constant, 2.0
$c_{\varepsilon 1}$ = turbulence modeling constant, 1.44
$c_{\varepsilon 2}$ = turbulence modeling constant, 1.92
c_{μ} = turbulence modeling constant, 0.09
D = turbulence diffusion term
d = distance to the wall, m
d_t = distance from field point to the wall trip point, m
F = switching function for Menter's k–ω model
f_{t1} = transition function
f_{t2} = transition function
f_w = turbulence modeling function
f_1 = turbulence modeling constant, 1.0
f_2 = turbulence modeling function
f_{β} = turbulence modeling function
f_{β^*} = turbulence modeling function
f_{μ} = turbulence modeling function
f_{v1} = near-wall turbulence damping function
f_{v2} = near-wall turbulence damping function
g = turbulence modeling function
k = specific turbulent kinetic energy, m^2/s^2
M = Mach number
n = time level
P = turbulence production term $\tau_{ij}(\partial \tilde{u}_i/\partial x_j)$
Pr_T = turbulent Prandtl number, 1.0
p = pressure, N/m^2, or transition region exponent
q = heat flux, W/m^2
Re = Reynolds number
R_N = vehicle nose radius, m
R_T = turbulence Reynolds number, $k^2/\nu\varepsilon$
r = turbulence modeling function
S = turbulence source term
$\hat{S}$ = strain rate for Spalart–Allmaras turbulence model
S_D = turbulence destruction source term
S_{ij} = strain rate tensor, $\frac{1}{2}(\partial \tilde{u}_i/\partial x_j + \partial \tilde{u}_j/\partial x_i)$, 1/s
S_P = turbulence production source term
S_t = turbulence transition source term
T = temperature, K
Tu = freestream turbulence intensity, %
t = time, s
U = conserved transport quantity
u_i = velocity in ith coordinate direction, m/s
u_t = tangential velocity, m/s
V = velocity magnitude, m/s
x = axial coordinate, m
x_i = ith coordinate direction, m
y = wall normal direction, m
α = angle of attack, deg, generic constant
β = turbulence modeling constant, generic constant, Roberts stretching parameter
β^* = turbulence modeling constant
Γ = turbulence intermittency; 0 = laminar, 1 = turbulent
γ = ratio of specific heats
$\hat{\gamma}$ = turbulence modeling constant
ΔU = velocity magnitude for Spalart–Allmaras model, m/s
Δx_t = grid spacing along the wall at the trip location, m
δ_{ij} = Kronecker delta function; 1 when $i = j$, otherwise 0
ε = specific dissipation rate, m^2/s^3, numerical error
η = curvilinear coordinate
θ_{cone} = cone half-angle, deg
κ = von Kármán constant, 0.41
Λ = transition modeling function
Λ^n = iterative convergence parameter
λ = transition modeling function
μ = absolute viscosity, Ns/m^2
$\hat{\mu}$ = absolute Spalart–Allmaras working variable, Ns/m^2
ν = kinematic viscosity, m^2/s
$\hat{\nu}$ = kinematic Spalart–Allmaras working variable, m^2/s

Presented as Paper 2000-0132 at the AIAA 38th Aerospace Sciences Meeting, Reno, NV, 10–13 January 2000; received 14 July 2000; revision received 30 January 2001; accepted for publication 5 February 2001.

*Senior Member of Technical Staff, Mail Stop 0825, Aerosciences and Compressible Fluid Mechanics Department, P.O. Box 5800; cjroy@sandia.gov. Member AIAA.

†Distinguished Member of Technical Staff, Mail Stop 0825, Aerosciences and Compressible Fluid Mechanics Department, P.O. Box 5800; fgblott@sandia.gov. Fellow AIAA.

ξ = curvilinear coordinate
ρ = density, kg/m^3
σ = turbulence modeling constant
τ_{ij} = turbulent stress tensor, m^2/s^2
φ = nonconserved transport quantity
χ = turbulence modeling parameter
χ^* = turbulence modeling function
Ω_{ij} = rotation tensor, $\frac{1}{2}(\partial\tilde{u}_i/\partial x_j - \partial\tilde{u}_j/\partial x_i)$, 1/s
ω = specific turbulent frequency, 1/s
ω_t = wall vorticity magnitude at the trip location, 1/s

Subscripts

E = exact value
e = end of transition
eff = effective value (turbulent plus laminar)
i, j, k = indices for tensor notation
k = quantity in turbulence kinetic energy equation
l = transition length
RE = Richardson Extrapolation value
ref = reference value
s = start of transition
T = turbulent quantity
t = transitional quantity
w = wall value
ε = quantity in turbulence dissipation rate equation
ω = quantity in turbulence frequency equation
1 = k–ω constant for Menter's model
2 = k–ε constant for Menter's model
∞ = freestream value

Superscripts

$+$ = quantity in wall coordinates
$\sim$ = Favre (density-weighted) averaging
— = Reynolds (time-based) averaging
$''$ = Favre fluctuating quantity

Introduction

THIS work is concerned with developing a capability to model high-speed compressible boundary layers with laminar, transitional, and turbulent flow regions. The approach uses one- and two-equation eddy-viscosity models to predict the turbulent flow. The same governing equations are presently being used to predict the transitional flow region where the onset to turbulent flow is specified and assumed to be known. The prediction of where onset to turbulent flow occurs is a research area that depends on an analysis of the flow stability, understanding of the flow disturbances outside the boundary layer, and a capability to predict the boundary-layer receptivity. The process of entraining disturbances into the boundary layer and producing perturbations that can be amplified is called receptivity.

The modeling of compressible transitional and turbulent flows is still an active area of research. A discussion of the physical mechanisms for transition to turbulence in supersonic and hypersonic boundary layers is given by Masad and Abid.[1] Singer[2] presents a review of modeling procedures for the transitional flow region, whereas Wilcox[3] gives a discussion of turbulence modeling for compressible flows. Huang et al.[4] discuss modifications for the standard turbulence models which are required to reproduce the compressible law of the wall for high-speed boundary layers.

The experimental data utilized in the current work are Van Driest's[5,6] compressible flat plate flow transformation as well as measurements from the Reentry F flight vehicle (see Ref. 7). The latter is a 5-deg half-angle cone with a small spherical nosetip and has flight data available for a wide range of hypersonic Mach numbers. In recent years, this experimental data set has been reevaluated with modern computational codes and is documented in Refs. 8–10. Aerothermal predictions have also been presented in these papers. Most of these solutions are for axisymmetric flow with the vehicle at 0-deg angle of attack, but full three-dimensional solutions have been obtained at actual flight angles of attack, for example, 0.14 deg at 24.4-km altitude. Although there are many details of this flight experiment that are not well defined, the overall heat transfer predictions are in reasonable agreement with the flight measurements.

The purpose of this paper is to assess the performance of several standard one- and two-equation turbulence models for hypersonic transitional flows. The Navier–Stokes equations were chosen instead of simpler formulations, for example, boundary-layer equations, because of their generality for more complex flows. The application of turbulence models to compressible flows is not always clear because most models were originally developed for incompressible flows. Formulations for incompressible flow are not applicable to compressible flow because some variables, for example, density and viscosity, have been assumed constant in the development. The turbulent transport equations are often written in substantial differential form, whereas conservation form is generally required in compressible Navier–Stokes codes. Problems with the formulation of the governing equations for compressible turbulence models in conservation form are discussed. For example, the form of the diffusion term in the Spalart–Allmaras[11,12] model is rewritten, and justification for the new form is given.

The Sandia advanced code for compressible aerothermodynamics research and analysis code (SACCARA)[13–16] is used for the results presented in this paper. For one-equation turbulence models, the SACCARA code has options for both the Baldwin–Barth[17] and Spalart–Allmaras[11,12] eddy-viscosity models. There is evidence that the use of the Baldwin–Barth model does not constitute a well-posed system of governing equations.[18] For boundary-layer and shear-layer flows, the solutions do not appear to converge to a unique solution as the mesh is refined. Therefore, there is more interest in using the Spalart–Allmaras model because it has proven to be numerically robust. Part of the present work is concerned with the evaluation of the Spalart–Allmaras model for high-speed flows and the simulation of the transition region with the Spalart–Allmaras model.

The SACCARA code also has options for three popular two-equation eddy-viscosity turbulence models: a low-Reynolds-number k–ε formulation and two k–ω models. The k–ε model employs the low-Reynolds-number modification of Nagano and Hishida[19] to allow integration to solid walls. The first k–ω formulation is the hybrid model of Menter,[20] which is a blending between a k–ω formulation (near solid walls) and a k–ε formulation (in shear layers and freestream flow). Menter proposed this hybrid model to take advantage of the accuracy of the k–ω model for wall-bounded flows and the k–ε model for free shear layers. The final model is the Wilcox k–ω model,[3] which was modified in 1998 to improve the predictive accuracy for shear flows. This model is referred to as the Wilcox (1998) model in the current work. The appropriate form of the two-equation eddy viscosity equations is important because the one-equation formulation can be developed from the two-equation transport relations. This approach may be used to determine the appropriate form of the transport equation for the one-equation models.

Two flow cases have been used to investigate the performance of the one- and two-equation eddy-viscosity models. The first case is the flow over a flat plate at Mach 8 with flow conditions corresponding to an altitude of 15 km, where the perfect-gas model is appropriate. The skin friction along the flat plate is used to judge the accuracy of the predictions through comparisons with the accurate laminar and turbulent results of Van Driest.[5,6] Squire[21] estimates the accuracy of the Van Driest-type turbulence correlations for compressible flows to be within $\pm 3\%$. The control of the transition location with the Spalart–Allmaras model has also been investigated.

The second case investigated is the flow over the Reentry F flight vehicle at Mach 20 and at an altitude of 24.4 km (80,000 ft), where real-gas effects are significant in the boundary layer and a small region in the inviscid flow due to nose bluntness. The measured heat transfer along the vehicle is used to judge the accuracy of the model predictions. The transition location is specified to give a reasonable match of the wall heat flux with the flight data. The solutions have been obtained on at least three mesh levels with the number of cells in each coordinate direction doubled for each mesh refinement. In addition, the solutions on each mesh are marched in time until the wall heat flux has obtained a steady-state value. The accuracy of the iterative solution relative to the steady-state

solution has been estimated for each model. The various uncertainties and assumptions in the flight experiment and prediction are discussed.

In this initial assessment of turbulence models for high-speed compressible flows, the investigation has been limited to turbulent boundary-layer flows with perfect- or real-gas properties and zero pressure gradient (the Reentry F case has been simulated with an equilibrium air model). The effects of chemical nonequilibrium with the introduction of species equations has not been addressed. For the present flow conditions, the effects of finite-rate chemistry should not be significant.

Favre-Averaged Transport Equation for Turbulence Models

The generic form of the turbulent transport equation in substantial derivative form[3] is

$$\bar{\rho}\frac{\mathrm{D}\varphi}{\mathrm{D}t} = D + S_P - S_D \tag{1}$$

where

$$D = D_1 - \bar{D}, \qquad D_1 = \frac{\partial}{\partial x_j}\left(\mu_{\text{eff}}\frac{\partial \varphi}{\partial x_j}\right)$$

For example, for a one-equation eddy viscosity model, the dependent variable φ is the kinematic eddy viscosity ν_T and the effective diffusion coefficient is μ_{eff}. In some models there are two parts to the diffusion term on the right-hand side of Eq. (1); D_1 is the first part of the diffusion term, which can be put in conservation form, and $\bar{D}$ is the remaining part. When $\bar{D}$ is included, it can take on several forms. The source term $S = S_P - S_D$ has a production part S_P and a dissipation part S_D. If the continuity equation is multiplied by φ and added to Eq. (1), the resulting equation is the generic transport equation in conservation form:

$$\frac{\partial U}{\partial t} + \frac{\partial}{\partial x_j}\left\{\bar{\rho}\tilde{u}_j\varphi - \mu_{\text{eff}}\frac{\partial \varphi}{\partial x_j}\right\} = \bar{D} + S_P - S_D \tag{2}$$

The dependent variable is now $U = \bar{\rho}\varphi$. This development utilizes Favre (tilde) and Reynolds (overbar) averaging. See Ref. 3 for notation and for details on the averaging procedures. For all results presented herein, a value of unity is assumed for the turbulent Prandtl number Pr_T.

One-Equation Turbulence Model

There have been a number of one-equation turbulence models developed that use a transport equation to solve for the eddy viscosity directly. The present work is focused on the Spalart–Allmaras model and a brief description is presented.

Spalart–Allmaras Model

The transport equation for determining the eddy viscosity with near-wall effects included has been developed by Spalart and Allmaras.[11,12] The governing equation form is slightly different from Eq. (1) and is

$$\bar{\rho}\frac{\mathrm{D}\varphi}{\mathrm{D}t} = D + S_P - S_D + S_t, \qquad \hat{\mu} = \frac{\mu_T}{f_{v1}} = \bar{\rho}\varphi \tag{3}$$

The dependent variable $\varphi = \hat{\nu} = \nu_T/f_{v1}$, where f_{v1} is a damping function used in the near-wall region and mainly in the viscous sublayer. This function and the right-hand-side terms will be defined later. The continuity equation is multiplied by φ and added to Eq. (3), which gives a transport equation in conservation form for the Spalart–Allmaras model in the form of Eq. (2),

$$\frac{\partial U}{\partial t} + \frac{\partial}{\partial x_j}\left\{\bar{\rho}\tilde{u}_j\varphi - \mu_{\text{eff}}\frac{\partial \varphi}{\partial x_j}\right\} = \bar{D} + S_P - S_D + S_t$$

$$U = \bar{\rho}\hat{\nu} = \bar{\rho}\varphi, \qquad \mu_{\text{eff}} = \frac{\mu + \hat{\mu}}{\sigma} \tag{4}$$

The right-hand side has contributions from a diffusion term as well as production, destruction, and trip terms. The four terms in the model are written as follows.

Diffusion-original form:

$$D = \bar{\rho}\frac{\partial}{\partial x_j}\left[\frac{\mu_{\text{eff}}}{\bar{\rho}}\frac{\partial \varphi}{\partial x_j}\right] + D_2 = D_1 + \bar{D}$$

$$\mu_{\text{eff}} = \frac{\mu + \hat{\mu}}{\sigma} = \bar{\rho}\frac{\nu + \varphi}{\sigma}, \qquad \bar{D} = D_2 - D_3$$

$$D_1 = \frac{\partial}{\partial x_j}\left[\mu_{\text{eff}}\frac{\partial \varphi}{\partial x_j}\right], \qquad D_2 = \frac{c_{b2}\bar{\rho}}{\sigma}\left(\frac{\partial \varphi}{\partial x_j}\right)\left(\frac{\partial \varphi}{\partial x_j}\right)$$

$$D_3 = \left(\frac{\mu_{\text{eff}}}{\bar{\rho}}\right)\frac{\partial \bar{\rho}}{\partial x_j}\frac{\partial \varphi}{\partial x_j}$$

Diffusion modified for compressible flow:

$$D = D_1 + D_2, \qquad \bar{D} = D_2, \qquad D_3 = 0$$

Production:

$$S_P = c_{b1}[1 - f_{t2}]\hat{S}\bar{\rho}\varphi, \qquad \hat{S} = \sqrt{2\Omega_{ij}\Omega_{ij}} + (\hat{\nu}/\kappa^2 d^2) f_{v2}$$

Destruction:

$$S_D = \left\{c_{w1} f_w - \left(c_{b1}/\kappa^2\right) f_{t2}\right\}\bar{\rho}(\varphi/d)^2$$

Trip term:

$$S_t = f_{t1}\bar{\rho}(\Delta U)^2$$

The quantity ΔU is simply the local velocity magnitude for fixed wall flows. In the formal transform of the transport equation into conservation form, the diffusion term includes a density gradient term, D_3. This term is zero when the transport equation [Eq. (4)] is developed from the compressible form of the k–ε transport equations[18,22] and is shown in the term labeled diffusion modified for compressible flow. This form of the diffusion term is used in the present work. Including this density gradient term has been found to cause stability problems for high-speed flows, while having negligible effect on the predictions. The model controls transition from laminar to turbulent flow with the use of the trip term. With this additional physics, the foregoing governing equation requires some additional terms and definitions for f_{t1} and f_{t2}, which involves the coefficients c_{t1}–c_{t4}. Except where noted, the standard values for the model constants and functions are used in the current work and are given by

$$f_{v1} = \frac{\chi^3}{\chi^3 + c_{v1}^3}, \qquad f_{v2} = 1 - \frac{\chi}{1 + \chi f_{v1}}, \qquad f_w = g\left(\frac{1 + c_{w3}^6}{g^6 + c_{w3}^6}\right)^{\frac{1}{6}}$$

$$\chi = \frac{\hat{\nu}}{\nu}, \qquad g = r + c_{w2}(r^6 - r), \qquad r = \frac{\hat{\nu}}{\hat{S}\kappa^2 d^2}, \qquad \sigma = \tfrac{2}{3}$$

$$c_{w1} = \frac{c_{b1}}{\kappa^2} + \frac{1 + c_{b2}}{\sigma} = 3.24, \qquad g_t = \min\left(0.1, \frac{\Delta U}{\omega_t \Delta x_t}\right)$$

$$f_{t1} = c_{t1} g_t \exp\left(c_{t2}\frac{\omega_t^2}{\Delta U^2}\left[d^2 + g_t^2 d_t^2\right]\right), \qquad f_{t2} = c_{t3} e^{-c_{t4}\chi^2}$$

Boundary Conditions for Spalart–Allmaras Model

At the wall, $\mu_T = 0$ or $\hat{\nu} = 0$. The freestream boundary condition for this model is the specification of the turbulent eddy viscosity μ_T. In the freestream there should be no production of the eddy viscosity, which requires that

$$f_{t2} = c_{t3} e^{-c_{t4}\chi^2} > 1$$

to turn off the production term in Eq. (6). The restriction on χ is

$$\chi = \hat{\nu}/\nu < \sqrt{(\ell n c_{t3})/c_{t4}} = 0.604$$

The restriction on the freestream eddy viscosity becomes

$$\mu_T/\mu < \chi f_{v1} = \chi \Big/ \left[1 + (c_{v1}/\chi)^3\right] = 3.713 \times 10^{-4} \qquad (5)$$

The freestream eddy viscosity as suggested by Spalart and Allmaras is $\tilde{\nu} < 1/2\nu$, which gives

$$\mu_T/\mu < \hat{\nu} f_{v1}/\nu = 1.746 \times 10^{-4}$$

Control of Laminar and Turbulent Flow with the Spalart–Allmaras Model

The governing equation has three terms that are influenced by the transition model. The complete source term (for the conservative formulation) is

$$S = \frac{c_{b2}\bar{\rho}}{Pr_T}\left(\frac{\partial \hat{\nu}}{\partial x_j}\right)^2 + c_{b1}[1 - \underline{f_{t2}}]\hat{S}U$$

$$- \left(c_{w1} f_w - \underline{c_{b1} f_{t2}/\kappa^2}\right)\bar{\rho}\left(\frac{\hat{\nu}}{d}\right)^2 + \underline{f_{t1}\bar{\rho}(\Delta U)^2} \qquad (6)$$

where the trip terms are underlined. The first term is part of the diffusion term and is included in the source term as it is evaluated numerically in an explicit manner. The second term is the production term, and it will produce or increase the eddy viscosity if $f_{t2} < 1$. The third term is the destruction term, and it will decrease the eddy viscosity if $c_{w1} f_w > c_{b1} f_{t2}/\kappa^2$. The fourth term is the trip term, and it will increase the eddy viscosity as $f_{t1} > 0$.

The model generally predicts turbulent flow everywhere when the trip terms are zero:

$$f_{t1} = 0 \quad \text{or} \quad c_{t1} = 0, \qquad f_{t2} = 0 \quad \text{or} \quad c_{t3} = 0$$

The flow can be made laminar everywhere with the following values of the trip terms:

$$f_{t1} = 0, \qquad f_{t2} \geq 1.0 \quad \text{or} \quad f_{t2} = c_{t3}\Lambda, \qquad \Lambda = e^{-c_{t4}\chi^2}$$

or

$$f_{t1} = 0, \qquad f_{t2} = 0, \qquad c_{b1} = 0$$

Several different approaches have been investigated to control transition and to replace the original trip model approach of Spalart–Allmaras.

Method 1 (f_{t2} Is Modified)

In this approach, the value of $f_{t1} = 0$ and $f_{t2} = c_{t3}(1 - \lambda)$, where λ varies from zero in the laminar flow region to one in the turbulent flow region. The parameter is increased smoothly and defines the transitional flow region. This method requires specification of the location and length of the transitional region.

Method 2 (c_{b1} Is Modified)

In this method, the trip terms f_{t1} and f_{t2} are set to zero. The coefficient c_{b1} is modified from the laminar flow region to the turbulent flow region as follows:

$$x < x_s: c_{b1} = 0, \qquad x > x_e: c_{b1} = 0.1355$$

$$x_s \leq x \leq x_e: c_{b1} = 0.1355\lambda^p, \qquad \lambda = (x - x_s)/(x_e - x_s)$$

where, for example, p may be chosen as 1 or 2. In this method, the location of the start of transitional flow x_s and end of transitional flow x_e are specified.

Method 3 [$c_{b1}(1 - f_{t2})$ Is Modified]

In this method the production term coefficient is modified by writing this term as $\alpha c_{b1}(1 - f_{t2})$. The parameter α increases from zero to one in the transitional flow region. From the definition of f_{t2}, the following is obtained:

$$\chi = \hat{\nu}/\nu = \sqrt{-\ell n[f_{t2}/c_{t3}]/c_{t4}} \qquad (7)$$

The production term switches sign when $f_{t2} = 1$, which gives a critical value of χ, which is $\chi^* = 0.604$. When $x < x_t$, set $\alpha = 0$, and there is no production of eddy viscosity upstream of the transition location x_t. When $x > x_t$, α is increased downstream toward one. This increase is controlled by setting

$$\alpha = 1 - f_{t2} = 1 - c_{t3}e^{-c_{t4}\chi^2}$$

When $x > x_t$ and $\chi \leq \chi^*$, then $\chi = \chi^*$. When $x > x_t$ and $\chi > \chi^*$, then χ is obtained from Eq. (7). In this method, only the single parameter x_t must be specified. The behavior of these three methods is discussed in the results section for the flat plate.

Two-Equation Turbulence Models

The standard method for specifying transition to turbulence is through analogy with the turbulence intermittency approach. The turbulence transport equations are solved over the entire domain, with a user-defined transition plane specified. Upstream of this plane, the effective viscosity is simply set to the laminar value, while downstream, the effective viscosity is the sum of the laminar and turbulent viscosities, that is,

$$\mu_{\text{eff}} = (1 - \Gamma)\mu + \Gamma\mu_T, \qquad \Gamma = \begin{cases} 0 & \text{laminar} \\ 1 & \text{turbulent} \end{cases}$$

For the remainder of this investigation, this transition specification method will be referred to as the step transition method.

High-Turbulent-Reynolds-Number k–ε Model

The high-Reynolds-number formulation[3] is appropriate for turbulent flows but is not appropriate in the near-wall region. It can be applied in the outer part of boundary layers and combined with an inner boundary layer approach near the wall to obtain a complete formulation. For the standard k–ε model, the turbulent kinetic energy equation for a compressible fluid can be rearranged into the form of Eq. (2), where the variables have the following values:

$$U = \bar{\rho}k = \bar{\rho}\varphi, \qquad \mu_{\text{eff}} = \mu_k, \qquad \bar{D} = 0$$

$$S_{Pk} = \bar{\rho}P, \qquad S_{Dk} = \bar{\rho}\varepsilon \qquad (8)$$

The standard form of the production term P for compressible flows[3] is

$$P = \tau_{ij}\frac{\partial \tilde{u}_i}{\partial x_j} \qquad (9)$$

where

$$\tau_{ij} = -\overline{u_i'' u_j''} = 2\nu_T\left(S_{ij} - \frac{1}{3}\frac{\partial \tilde{u}_k}{\partial x_k}\delta_{ij}\right) - \frac{2}{3}k\delta_{ij} \qquad (10)$$

However, for the k–ε model, the compressible production term is approximated by the incompressible contribution only, that is,

$$P \approx \nu_T\left(\frac{\partial \tilde{u}_i}{\partial x_j} + \frac{\partial \tilde{u}_j}{\partial x_i}\right)\frac{\partial \tilde{u}_i}{\partial x_j} \qquad (11)$$

The effective viscosities are

$$\mu_k = \mu + \mu_T/\sigma_k, \qquad \mu_\varepsilon = \mu + \mu_T/\sigma_\varepsilon$$

$$\text{where} \quad \mu_T = c_\mu f_\mu \bar{\rho}k^2 \Big/ \varepsilon \qquad (12)$$

For the high-Reynolds-number model, $f_\mu = 1$. The transport equation for dissipation of turbulent kinetic energy can also be put in the form of Eq. (2), where the variables have the following values:

$$U = \bar{\rho}\varepsilon = \bar{\rho}\varphi, \qquad \mu_{\text{eff}} = \mu_\varepsilon, \qquad \bar{D} = 0$$

$$S_{P\varepsilon} = c_{\varepsilon 1} f_1 \bar{\rho}(\varepsilon/k)P, \qquad S_{D\varepsilon} = c_{\varepsilon 2} f_2 \bar{\rho}(\varepsilon^2/k) \qquad (13)$$

The constants in the foregoing equations use the standard values, $\sigma_k = 1.0$ and $\sigma_\varepsilon = 1.3$.

Low-Turbulent-Reynolds-Number k–ε Model

The Nagano and Hishida model[19] was developed for incompressible flow and is included in the current formulation. The model uses

the following damping function in the eddy viscosity relation given in Eq. (12):

$$f_\mu = [1 - \exp(-y^+/26.5)]^2$$

The source term for the turbulent kinetic energy equation (8) is

$$S = \bar{\rho}P - \bar{\rho}\varepsilon + \tilde{D}$$

Again, the production term has been approximated with by the incompressible form given in Eq. (11). The source term for the dissipation rate equation is

$$S = (\varepsilon/k)(c_{\varepsilon 1} f_1 \bar{\rho} P - c_{\varepsilon 2} f_2 \bar{\rho}\varepsilon) + \tilde{E}$$

The parameters in these source terms are

$$f_2 = 1 - 0.3e^{-R_T^2}, \qquad R_T = \frac{k^2}{\nu\varepsilon}$$

$$\tilde{D} = -2\mu\left(\frac{\partial\sqrt{k}}{\partial y}\right)^2, \qquad \tilde{E} = \mu\nu_T(1 - f_\mu)\left(\frac{\partial^2 \tilde{u}_t}{\partial y^2}\right)^2$$

where the variables $\tilde{D}$ and $\tilde{E}$ use boundary-layer-type derivatives normal to the wall and $\tilde{E}$ requires the tangential velocity component $\tilde{u}_t$.

The Nagano–Hishida and the Launder–Sharma[23] low-Reynolds k–ε turbulence models have been used by Theodoridis et al.[24] to predict transitional flow. They have investigated a flat plate flow experiment, where the freestream turbulent intensity was approximately 3 and 6%. The two turbulence models were used to model the laminar to turbulent bypass transition in which the freestream turbulence determines where the transition to turbulent flow occurs. For this bypass transition case, the Nagano–Hishida model predicts transition to turbulent flow too near the leading edge, whereas the Launder–Sharma model predictions are in reasonable agreement with the experimental data. Of course, neither of these turbulence models was developed to predict where transition will occur in a flow; the performance of the Launder–Sharma model in predicting the location of transition is fortuitous. The failure of the Nagano–Hishida model for transitional flow requires caution in the application of this model, and a procedure is required to have the model turned on at the appropriate location.

Menter k–ω Model

Two different two-equation turbulence models are described that solve equations for the turbulent kinetic energy k and the frequency of turbulent fluctuations ω. The Menter k–ω model[20] is a hybrid model that uses a blending function to combine the best aspects of both the k–ω and the k–ε turbulence models. Near solid walls, a k–ω formulation is used that allows integration to the wall without any special damping or wall functions. Near the outer edge of the boundary layer and in shear layers, the model blends into a transformed version of the k–ε formulation, thus providing good predictions for free shear flows.

The Menter k–ω model can be written in the form of Eq. (2) for both the turbulent kinetic energy equation,

$$U = \bar{\rho}k = \bar{\rho}\varphi, \qquad \mu_{\text{eff}} = \mu_k, \qquad \bar{D} = 0$$
$$S_{Pk} = \bar{\rho}P, \qquad S_{Dk} = \beta^*\bar{\rho}k\omega \tag{14}$$

and the turbulent frequency equation,

$$U = \bar{\rho}\omega = \bar{\rho}\varphi, \qquad \mu_{\text{eff}} = \mu_\omega, \qquad \bar{D} = 2\bar{\rho}(1 - F)\sigma_{\omega 2}\frac{1}{\omega}\frac{\partial k}{\partial x_j}\frac{\partial \omega}{\partial x_j}$$
$$S_{P\omega} = \bar{\rho}\frac{\hat{\gamma}}{\nu_T}P, \qquad S_{D\omega} = \beta\bar{\rho}\omega^2 \tag{15}$$

The cross-diffusion term $\bar{D}$ in Eq. (15) arises due to the transformation of the ε equation into an equation for ω. The compressible form of the production term from Eq. (9) is employed. The effective viscosities are given by

$$\mu_k = \mu + \sigma_k\mu_T, \qquad \mu_\omega = \mu + \sigma_\omega\mu_T, \qquad \text{where} \quad \mu_T = \bar{\rho}k/\omega \tag{16}$$

and the model constants are blended values of the k–ω and k–ε parameters. For example, for the constant β,

$$\beta = F\beta_1 + (1 - F)\beta_2$$

where F varies from unity at the wall to zero outside wall boundary layers and a subscript 1 denotes k–ω constants and a 2 denotes k–ε constants. The values for these constants are

$$\sigma_{k1} = 0.5, \qquad \sigma_{\omega 1} = 0.5, \qquad \beta_1 = 0.075$$
$$\beta^* = 0.09, \qquad \hat{\gamma}_1 = \left(\beta_1/\beta^*\right) - \left(\sigma_{\omega 1}\kappa^2/\sqrt{\beta^*}\right) = 0.553$$
$$\sigma_{k2} = 1.0, \qquad \sigma_{\omega 2} = 0.856, \qquad \beta_2 = 0.0828$$
$$\beta^* = 0.09, \qquad \hat{\gamma}_2 = \left(\beta_2/\beta^*\right) - \left(\sigma_{\omega 2}\kappa^2/\sqrt{\beta^*}\right) = 0.44$$

Wilcox (1998) k–ω Model

For the Wilcox (1998) k–ω model,[3] the terms in Eq. (2) for the turbulent kinetic energy equation are

$$U = \bar{\rho}k = \bar{\rho}\varphi, \qquad \mu_{\text{eff}} = \mu_k, \qquad \bar{D} = 0$$
$$S_{Pk} = \bar{\rho}P, \qquad S_{Dk} = \beta^* f_{\beta^*}\bar{\rho}k\omega \tag{17}$$

and for the turbulent frequency equation are

$$U = \bar{\rho}\omega = \bar{\rho}\varphi, \qquad \mu_{\text{eff}} = \mu_\omega, \qquad \bar{D} = 0$$
$$S_{P\omega} = \bar{\rho}(\hat{\gamma}/\nu_T)P, \qquad S_{D\omega} = \beta f_\beta \bar{\rho}\omega^2 \tag{18}$$

where

$$\hat{\gamma} = 0.52, \qquad \sigma_k = \sigma_\omega = 0.5, \qquad \beta^* = 0.09$$

$$f_{\beta^*} = \begin{cases} 1, & \chi_k \le 0, \\ \dfrac{1 + 680\chi_k^2}{1 + 400\chi_k^2}, & \chi_k > 0, \end{cases} \qquad \chi_k \equiv \frac{1}{\omega^3}\frac{\partial k}{\partial x_j}\frac{\partial \omega}{\partial x_j}$$

$$\beta_0 = 0.072, \qquad f_\beta = \frac{1 + 70\chi_\omega}{1 + 80\chi_\omega}, \qquad \chi_\omega \equiv \left|\frac{\Omega_{ij}\Omega_{jk}S_{ki}}{(\beta^*\omega)^3}\right|$$

The production term P and the eddy-viscosity definitions are given in Eqs. (9) and (16), respectively. This formulation is a modification to an earlier Wilcox k–ω model[25] and is designed to improve model predictions for certain shear-layer flows and to reduce the solution sensitivity to freestream ω values.

Boundary Conditions for the Two-Equation Turbulence Models

For all three two-equation models, the turbulent kinetic energy k is specified to be zero at solid surfaces. The specific dissipation rate ε is also set to zero at walls. For the k–ω models, the omega value for the first cell off the wall ω_1 is set to

$$\omega_1 = 6\nu/\beta(\Delta y)^2 \tag{19}$$

where Δy is the distance from the cell center to the wall. The wall value is set to

$$\omega_w = 10\left[6\nu_w/\beta(\Delta y)^2\right] \tag{20}$$

The interior ghost cell value for the turbulent frequency, ω_{-1}, is then set so that the second derivative of ω at the wall is zero, that is,

$$\omega_{-1} = 2\omega_w - \omega_1 = \frac{6(20\nu_w - \nu_1)}{\beta(\Delta y)^2} \tag{21}$$

where ν_1 is the molecular viscosity in the first interior cell off the wall.

The method for determining the freestream turbulence properties for the two-equation models is given as follows. The specification of a freestream turbulence intensity Tu is used to determine the turbulent kinetic energy in the freestream from

$$k = (1.2/2)[(Tu/100)V_\infty]^2 \tag{22}$$

where, for example, $Tu = 10$ corresponds to a freestream turbulence intensity of 10%. The dissipation and turbulence frequency are then determined by specifying the turbulent viscosity μ_T, that is,

$$\varepsilon = C_\mu \rho k^2 / \mu_T \qquad \text{or} \qquad \omega = \rho k / \mu_T \tag{23}$$

Flow Predictions for Flat Plate

Flow over a flat plate has been chosen as a high-speed test case to illustrate the behavior of the laminar/turbulent flow results obtained with the one- and two-equation turbulence models. The test case is Mach 8 flow over a flat plate with a wall temperature of $T_w = 1000$ K and freestream conditions corresponding to an altitude of 15 km. For this case, the temperature in the flow is sufficiently low that perfect-gas assumption with $\gamma = 1.4$ is reasonable.

Freestream Flow Conditions

The freestream conditions[26] for the flat plate case are

$$p_\infty = 1.21114 \times 10^4 \text{ N/m}^2, \qquad T_\infty = 216.65 \text{ K}$$

$$\rho_\infty = 0.19475 \text{ kg/m}^3, \qquad a_\infty = \sqrt{\gamma p_\infty / \rho_\infty} = 295.07 \text{ m/s}$$

$$V_\infty = a_\infty M_\infty = 2360.54 \text{ m/s}$$

$$\mu_\infty = \frac{1.458 \times 10^{-6} T_\infty^{\frac{3}{2}}}{(T_\infty + 110.4)} = 1.4216 \times 10^{-5} \text{ Ns/m}^2$$

where Sutherlands law is used for the absolute viscosity. For the Spalart–Allmaras model, the restriction on the freestream eddy viscosity is determined by Eq. (5), which gives

$$\mu_{T\infty} < 5.27 \times 10^{-9} \text{ Ns/m}^2$$

for the Mach 8 flat plate flow case. The freestream eddy viscosity for all models was, thus, chosen as

$$\mu_{T\infty} < 1.0 \times 10^{-9} \text{ Ns/m}^2$$

unless indicated otherwise. For the two-equation models, the further specification of a freestream turbulence intensity of 0.01% was used to determine the turbulent kinetic energy in the freestream from Eq. (22).

Computational Mesh for the Flat Plate

A parabolic mesh has been used around the flat plate with the (x, y) Cartesian coordinate system fixed at the leading edge. The parabolic mesh topology was chosen because it allows for easy clustering at the leading edge, which helps to mitigate the effects of the leading-edge singularity. The computational coordinates ξ and η are related to the Cartesian coordinates as follows:

$$x = \alpha(\xi^2 - \eta^2), \qquad y = 2\alpha\xi\eta, \qquad \alpha = 0.05$$

$$0 \le \xi \le \xi_{\max}, \qquad 0 \le \eta \le 1, \qquad \xi_{\max} = \sqrt{1 + 1/\alpha}$$

The value of $\xi_{\max}$ has been determined by setting $x = 1$ at $\eta = 1$. This gives a mesh that is slightly longer than 1 m along the flat plate. A uniform mesh is used in the ξ coordinate direction whereas a nonuniform mesh spacing is used in the η coordinate direction. The mesh spacing has been determined with the lower boundary stretching transformation of Roberts[27] (see also Ref. 28). Most of the results have been obtained with 80×160 cells. A coarser mesh of 40×80 and a finer mesh of 160×320 have been used to show that the 80×160 mesh provides results sufficiently accurate for the figures presented. A Roberts stretching parameter of $\beta = 1.001$ has been used for the one-equation models. This choice for β gives maximum y^+ values at the wall of approximately 2.3 for the coarse 40×80 mesh. As expected, the maximum allowable y^+ values for the two-equation models were found to be much smaller than for the one-equation models, with the larger values resulting in convergence problems. Thus, for the two-equation models, a stretching parameter of $\beta = 1.00007$ was used giving $y^+ \le 0.2$ at the wall for the coarse mesh.

Flat Plate Results with the Step Transition Method

For the freestream conditions and meshes just specified, the laminar/turbulent flow has been calculated with the SACCARA code and compared to the accurate laminar and turbulent results obtained for this case by Van Driest.[5,6] The uncertainty in the skin friction for Van Driest-type correlations for turbulent compressible flows was recently estimated to be ±3% (see Ref. 21). The step transition method is used where the laminar viscosity is the sole contributor to the effective viscosity upstream of the transition plane. For this case, the Spalart–Allmaras model has the f_{t1} trip term set to zero. The transition location was specified at $Re_{x_t} = 3.84 \times 10^6$ ($x_t = 0.1196$ m). The choice of the transition location is somewhat arbitrary because the results will be compared to both laminar and turbulent flow theory. The L_2 norms of the residuals for both the momentum equations and the turbulence equations were reduced at least eight orders of magnitude in each case, suggesting that the results for the flat plate problem are not influenced by iterative convergence error.

Skin-friction profiles have been obtained using all five turbulence models for the Mach 8 flat plate case. The Baldwin–Barth and both k–ω models give transition at the specified transition plane for the given freestream turbulence levels as shown in Fig. 1. To move the transition point to the desired location, the freestream eddy viscosity had to be increased to 1×10^{-6} Ns/m^2 for the Spalart–Allmaras model, and the turbulence intensity had to be increased to 0.1% for the low-Reynolds-number k–ε model (see Fig. 2). All of the models

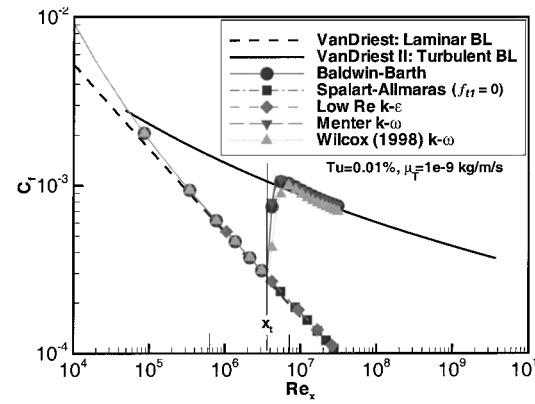

Fig. 1 Transition location with one- and two-equation turbulence models for Mach 8 flat plate flow with the step transition method.

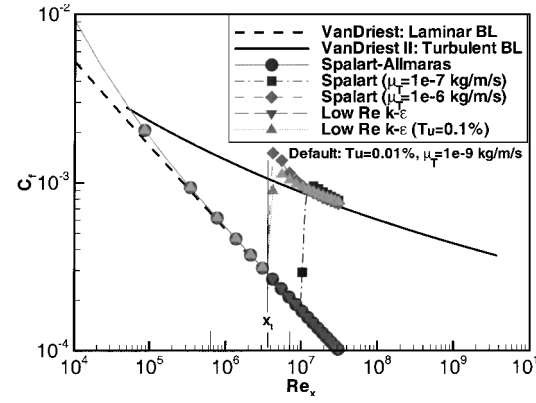

Fig. 2 Transition location for various freestream turbulence levels with the Spalart–Allmaras and k–ε turbulence models for Mach 8 flat plate flow (step transition method).

that correctly predict turbulent flow downstream of the transition point also predict skin friction in this region in agreement with the theory. Note that the current work does not address the sensitivity of the results to freestream turbulence levels.

Modified Transition Results for Spalart–Allmaras Model

Solutions have been obtained with both of the Spalart–Allmaras trip functions f_{t1} and f_{t2} set to zero. For this case, the flow is turbulent along the flat plate with the freestream eddy viscosity μ_T varying from 10^{-9} to 10^{-5} Ns/m^2. Thus, with the trip functions set to zero, the sensitivity of the transition location to the freestream eddy viscosity is greatly reduced. Solutions have been obtained with the trip function f_{t2} included and f_{t1} set to zero. For this case, the flow transition location is dependent on the freestream eddy viscosity. When the eddy viscosity is 10^{-9} Ns/m^2, the flow remains laminar over the length of the flat plate. With the freestream eddy viscosity set to 10^{-7} Ns/m^2, the transition location is at $Re_x \approx 10^7$, and with freestream eddy viscosity of 10^{-5} Ns/m^2, the transition location is at $Re_x \approx 2 \times 10^{-5}$. As already discussed, numerical solutions show that the flow can be maintained laminar by making the production term S_P zero by setting $c_{b1} = 0$ with the trip functions f_{t1} and f_{t2} set to zero.

The complete Spalart–Allmaras model has trip terms included to control the transition location, but the formulation is not intended to model the transition flow region. The behavior of this model has been investigated with the results for the local skin friction given in Fig. 3, where the trip location x_t is specified ($x_t = 0.11964$ m). The numerical predictions show that transition does not occur at the desired location and varies as the freestream eddy viscosity is increased above a value of approximately 10^{-9} Ns/m^2. For these high-speed flows, it is difficult to control the transition location with the suggested trip model. In addition, there is no control of the length of the transition region. Because of these experiences with the behavior of the Spalart–Allmaras trip model, different approaches have been investigated.

Three methods have been investigated to control the transition location and the length of transition as already described. There are two parameters x_t and x_l introduced to control the transition behavior. The parameter x_t is at the middle of the transition region, $x_s = x_t - x_l$ is the location upstream where transition starts, and the location downstream $x_e = x_t + x_l$ where the transition region ends and the flow becomes fully turbulent. The values for these parameters are chosen as $x_t = 0.1196$ m, $x_l = 0.1$ m, and $Re_{x_t} = 3.84 \times 10^6$, and these locations are also indicated in Fig. 4.

The results for the skin friction with the three proposed approaches for modeling transition have been investigated. All of the methods remain laminar a significant distance after the specified start of transition. With method 1, where the trip function f_{t2} is modified, transition occurs downstream of the desired location with very rapid transition onset. With method 2, where the production coefficient c_{b1} is modified, transition occurs near the desired location with a reasonable variation of the skin friction in the transition region. With method 3, where the production term coefficient $c_{b1}(1 - f_{t2})$ is modified, transition occurs downstream of the desired transition location with very rapid transition onset. From this investigation, it is concluded that method 2 provides a reasonable technique to specify the transition location with limited control over the transition region length. The results for method 2 are presented in Fig. 4. When λ varies linearly over the transition region ($p = 1$), there is better control. The transition control method 2 appears to be insensitive to the freestream eddy viscosity.

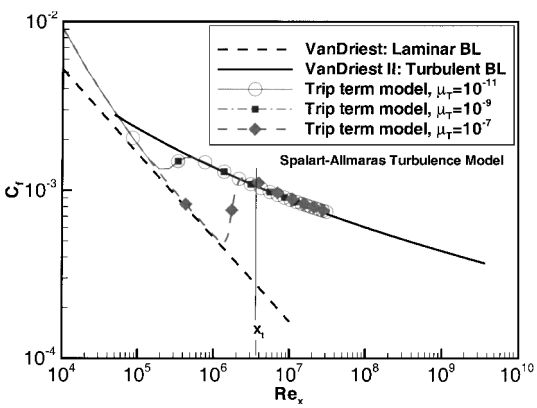

Fig. 3 Transition location for different freestream eddy viscosities with the Spalart–Allmaras turbulence model (f_{t1} and f_{t2} terms included) for Mach 8 flat plate flow.

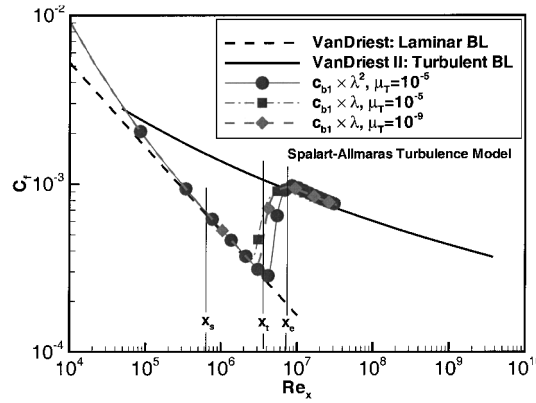

Fig. 4 Transitional flow behavior for Spalart–Allmaras (method 2) with various freestream eddy viscosities for Mach 8 flat plate flow.

Flow Predictions for Reentry F Vehicle

Reentry F Description and Experimental Results

The Reentry F flight experiment[7] was performed in 1968 to provide measurements of wall heat transfer rates at reentry flow conditions that cannot be obtained in ground-based experimental facilities. The data are for the flow over a slender conical vehicle where there is only a small amount of surface ablation localized at the nosetip. The boundary-layer flow is laminar, transitional, or turbulent depending on the altitude and location along the body surface. The Reentry F vehicle was a 5-deg half-angle sphere–cone with an initial nose radius of 0.00254 m, and the vehicle length is 4.0 m. A graphite nosetip extended for the first 0.1915 m followed by a conical beryllium frustum. The heat transfer measurements were obtained at altitudes between 36.6 and 18.3 km. The data at a flight time of 456.0 s or an altitude of 24.4 km are used to validate the turbulence model predictions. Although this flight experiment provides exceptional data, there are many aspects of the flow conditions, body orientation, body shape, and wall surface temperature that are not completely or precisely known. Additional details of the flight experiment are given by Wright and Zoby.[7]

The flow conditions at an altitude of 24.4 km are analyzed most often and are chosen for the present investigation. The freestream conditions used herein are based on the U.S. Standard Atmosphere, 1976,[26] and are

$$M_\infty = 19.97, \qquad \alpha = 0 \text{ deg}, \qquad \rho_\infty = 0.043523 \text{ kg/m}^3$$

$$T_\infty = 221.034 \text{ K}, \qquad T_w = 500 \text{ K}, \qquad p_\infty = 2761.41 \text{ N/m}^2$$

$$V_\infty = 5951.858 \text{ m/s}, \qquad a_\infty = 298.04 \text{ m/s}, \qquad Tu = 0.01\%$$

$$\mu_\infty = 1.445 \times 10^{-5} \text{ Ns/m}^2, \qquad \mu_T = 3.3227 \times 10^{-14} \text{ Ns/m}^2$$

An assumed turbulence intensity Tu is used in the determination of the turbulent kinetic energy for the two-equation models. Note that there is some amount of uncertainty in the specification of these properties. In addition, the experimentally reported angle of attack was 0.14 deg, whereas 0 deg is assumed herein so that the axisymmetric flow assumption can be used.

Because of ablation, the nose radius increases to 0.00343 m at an altitude of 24.4 km. This result is an estimated value from an ablation analysis of the nosetip.[10] For the present analysis, it is assumed that the nosetip shape remains a sphere–cone after ablation with the same cone half-angle as the conical vehicle, which is $\theta_{\text{cone}} = 5$ deg.

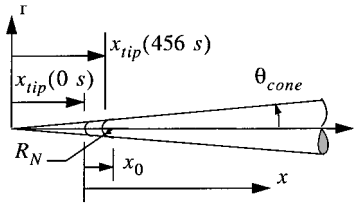

Fig. 5 Diagram of the Reentry F flight vehicle with the nosetip location at times t = 0 and 456 s in the flight trajectory indicated.

The nosetip is shown in Fig. 5. The origin in Fig. 5 is located at the virtual tip of the conical vehicle. For the approximated sphere–cone configuration in the Reentry F vehicle simulation, the location of the original nosetip and ablated nosetip 456 s into the flight trajectory is specified as

$$x_0 = 0.012752\ \text{m}, \qquad x_{\text{tip}}(0\ \text{s}) = 0.026603\ \text{m}$$

$$x_{\text{tip}}(456\ \text{s}) = 0.035925\ \text{m}$$

In previous analyses of this vehicle, the coordinate x is defined as the axial distance without a clear definition of the origin location given in many cases. Some figures indicate that the origin is located at the ablated nose of the body. The axial location x in this paper is measured from the nosetip of the unablated vehicle. However, due to the small amount of ablation, the uncertainty in the location of the axial heat flux measurements has a negligible impact on the results presented.

Because of the high velocities, the gas temperature is more than 6000 K in the nosetip region with dissociation of the oxygen and nitrogen occurring. Downstream of the nose, on the conical portion of the vehicle, the temperature immediately behind the oblique shock is 420 K, and perfect-gas flow occurs. However, in the boundary layer, the viscous dissipation increases the gas temperature to approximately 3000 K, and dissociation of oxygen occurs. At 24.4 km, the chemical reactions are sufficiently fast that the air is assumed to be in local thermochemical equilibrium. There is some ablation of the nosetip, which introduces chemical species from the ablation products into the boundary-layer flow. Because the amount of ablation is small, this influence has been neglected.

Predictions of Wall Heat Flux for Reentry F Vehicle

Simulation Code and Model Approach

The flow around the Reentry F vehicle has been calculated with the SACCARA[13–16] Navier–Stokes code. This investigation is concerned with obtaining accurate numerical solutions of the wall heat flux based on the input conditions to the code and models used in the simulation. The wall heat flux predictions are then compared with the flight measurements at an altitude of 24.4 km. The solution is for the flow over the ablated vehicle. The small angle of attack of the vehicle (0.14 deg) is neglected, and the flow is assumed to be axisymmetric. The solutions use a gas model of air in local thermochemical equilibrium, and the flow is laminar over the front part of the body. The flow transitions to turbulent flow at a specified location. The turbulent flow has been modeled with the Baldwin–Barth and Spalart–Allmaras one-equation eddy-viscosity approaches and the low-Reynolds-number k–ε, Menter k–ω, and Wilcox (1998) k–ω two-equation turbulence models. The iterative convergence has been examined to assess the accuracy of the steady-state solutions. Various levels of grid refinement were used to assess the spatial convergence errors of the numerical solutions. For the Spalart–Allmaras turbulence model, solutions have been obtained on four mesh levels: 100 × 40 cells (mesh 0-f), 200 × 80 cells (mesh 1-f), 400 × 160 cells (mesh 2-f), and 800 × 320 cells (mesh 3-f). The number of grid points are given along the surface and normal to the surface, respectively. For the two-equation models, solutions have been obtained on three mesh levels: 130 × 40 cells (mesh 0-2eq), 260 × 80 cells (mesh 1-2eq), and 520 × 160 cells (mesh 2-2eq).

Transition Model

As already discussed, the basic SACCARA code treats the transition process by setting the effective viscosity to the laminar value upstream of a specified transition plane, whereas downstream of this plane the effective viscosity is the sum of both the laminar and turbulent viscosities. This approach has been used with the Baldwin–Barth one-equation eddy-viscosity model and all two-equation models. The transition plane is specified to be perpendicular to the vehicle axis and located at $x = 2.6$ m. With the Spalart–Allmaras one-equation eddy viscosity model, a different approach has been implemented as described earlier, with $x_s = 1.8844$ m and $x_e = 2.8844$ m. From the results of the investigation of the flat plate flow case, it was concluded that method 2 (coefficient c_{b1} is varied) is the best approach to control the transition process with the Spalart–Allmaras model at this time.

Iterative Convergence of the Numerical Solutions

The L_2 norms of the momentum and turbulence transport equations exhibited oscillatory behavior after only a two or three order of magnitude drop; thus, another method was needed to monitor convergence. The iterative convergence has been initially determined by plotting the wall heat flux at various number of time steps and assuming convergence has been obtained when there is no noticeable change in the results. This method is shown in Fig. 6 for the 400 × 160 cell mesh (mesh 2-f) with the Spalart–Allmaras turbulence model. The laminar flow region takes the longest time to converge because there is a very fine mesh in the wall region. With mesh 2-f, the wall heat flux appears to have no significant changes after 25,000 time steps. However, these results are misleading. A more careful analysis has been performed to quantify the iterative convergence error.

The accuracy of the wall heat flux q^n relative to the steady-state value is determined by expressing the numerical solution at time t^n as

$$q^n = q(t^n) = q_E + \varepsilon^n \tag{24}$$

The exact steady-state value of the wall heat flux is q_E and the convergence error at time t^n is ε^n. The convergence error of the SACCARA code has been observed to have an exponential decrease in time, which gives the following variation as the solution approaches a steady state:

$$\varepsilon^n = \alpha e^{-\beta t^n} \tag{25}$$

where α and β are constants. Equations (24) and (25) may be combined and rewritten as

$$\beta t^n = \ell n \alpha - \ell n \left(q^n - q_E\right) \tag{26}$$

Equation (26) is evaluated at three time levels, $(n-1)$, n, and $(n+1)$, and the three relations are used to eliminate α and obtain

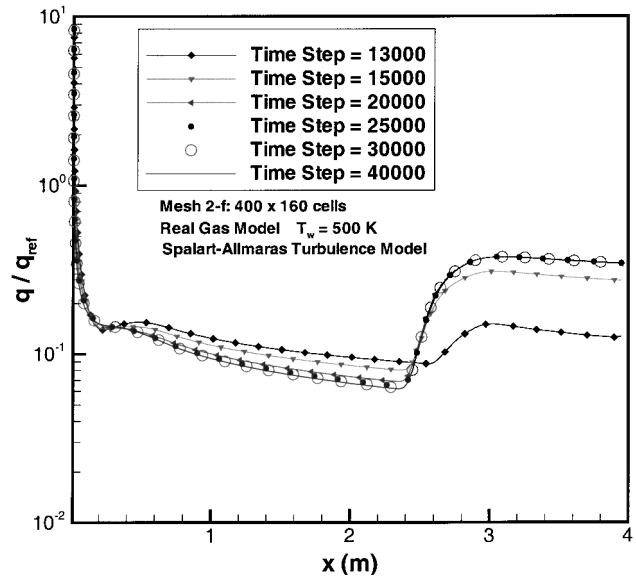

Fig. 6 Iterative convergence of surface heat flux on mesh 2-f with the Spalart–Allmaras turbulence model.

$$\beta(t^n - t^{n-1}) = \ln\left[\left(q^{n-1} - q_E\right)/\left(q^n - q_E\right)\right]$$

$$\beta(t^{n+1} - t^n) = \ln\left[\left(q^n - q_E\right)/\left(q^{n+1} - q_E\right)\right]$$

If the time increments are equal, then $(t^n - t^{n-1}) = (t^{n+1} - t^n)$ and the preceding equation becomes

$$\left(q^{n-1} - q_E\right)\left(q^{n+1} - q_E\right) = \left(q^n - q_E\right)^2$$

The exact steady-state value of the wall heat flux is solved for in the preceding equation, which gives

$$q_E = \frac{q^n - \Lambda^n q^{n-1}}{1 - \Lambda^n}, \qquad \text{where} \quad \Lambda^n = \frac{(q^{n+1} - q^n)}{(q^n - q^{n-1})} \tag{27}$$

The iterative convergence error becomes

$$\varepsilon^n = -(q^{n+1} - q^n)/(1 - \Lambda^n)$$

and the convergence error relative to the exact steady-state value becomes

$$\%\ \text{error of}\ q^n = -100\left[\frac{q^{n+1} - q^n}{q^n - \Lambda^n q^{n-1}}\right] \tag{28}$$

The foregoing results are related to the approach of Ferziger and Peric[29,30] for determining the convergence error of the numerical iterative solution of difference equations, but their results have been obtained with a different approach. In their work, the parameter Λ^n is the spectral radius (or the magnitude of the largest eigenvalue) of the iteration matrix. If the eigenvalues are complex, then the present approach is not appropriate. The complex eigenvalue case has been considered by Ferziger and Peric in Ref. 30.

The described procedure is illustrated for the wall heat flux solution at $x \approx 2.15$ m (where the flow is laminar) using the Spalart–Allmaras simulations. The error is shown in Fig. 7 for the four mesh levels. The local errors obtained from Eq. (28) based on time levels $(n-1)$, n, and $(n+1)$ are indicated by the symbols. The lines in Fig. 7 represent the error obtained from the best estimate of the exact solution given by Eq. (27). This best estimate is determined from the final three iteration levels of the solution. Because of the expense of the fine grid mesh 3-f calculation (800×320 cells), the converged mesh 2-f results were used to provide an initial starting solution for this case. The initial solution results on mesh 2-f (shown in Fig. 6) appeared converged at 25,000 iterations; however, this error analysis indicates that the local iterative errors are on the order of 4% (see Fig. 7). An additional 15,000 iterations were needed to reduce the error down to 0.2%. The iterative solution errors are much smaller than the spatial solution errors, as will be demonstrated.

The iterative convergence for the two-equation turbulence models was also examined for the three mesh levels. Results of the iterative

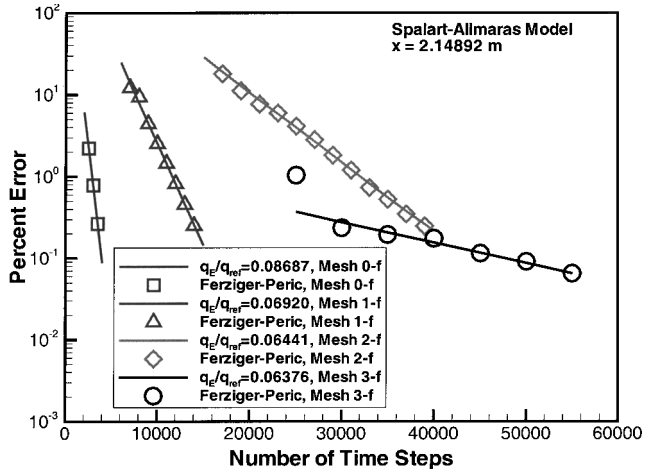

Fig. 7 Iterative convergence error of the surface heat flux for the Spalart–Allmaras model at $x = 2.14892$ m with mesh f.

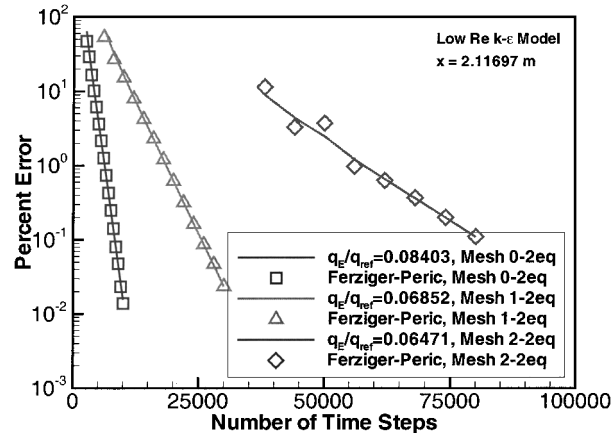

Fig. 8 Iterative convergence error of the surface heat flux for the k–ε model at $x = 2.11697$ m with mesh 2eq.

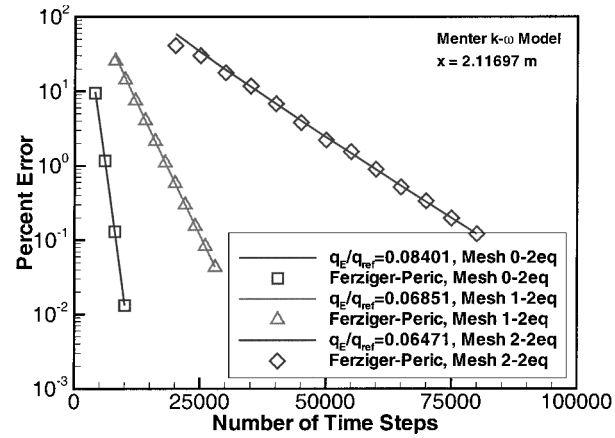

Fig. 9 Iterative convergence error of the surface heat flux for the Menter k–ω model at $x = 2.11697$ m with mesh 2eq.

error analysis at $x \approx 2.12$ m are presented for the low-Reynolds-number k–ε model (Fig. 8), the Menter k–ω model (Fig. 9), and the Wilcox (1998) k–ω model (Fig. 10). A larger number of iterations were required due to the finer mesh requirements for the two-equation turbulence models (mesh 2eq) vs the one-equation models (mesh f). The two-equation results were also converged to less than 0.1% error.

Spatial Convergence of the Numerical Solutions

Spatial convergence has been assessed from the steady-state solutions with the Spalart–Allmaras turbulence model on the four meshes. The wall heat fluxes are obtained from mesh 0-f (100×40 cells) to mesh 3-f (800×320 cells). The Richardson Extrapolation procedure (see Ref. 31) has been used to obtain a more accurate result from the relation

$$q_{\text{RE}} = q_3 + (q_3 - q_2)/3 \tag{29}$$

The preceding relation assumes that the numerical scheme is second order both within the domain and at the boundaries. Although recent findings[32,33] have shown that flows with captured shock waves will tend toward first order as the mesh is refined, analyses that account for mixed first- and second-order behavior are beyond the scope of the current work. The results from Ref. 33 indicate that the application of standard second-order Richardson Extrapolation to mixed-order problems can provide good estimates of the exact solution. The accuracy of the solutions on the four meshes has been estimated with the exact solution approximated with q_{RE}, which gives the solution error as

$$\%\ \text{error of}\ q_M = 100(q_M - q_{\text{RE}})/q_{\text{RE}}$$

where $M = 0$, 1, 2, or 3 refers to the mesh level.

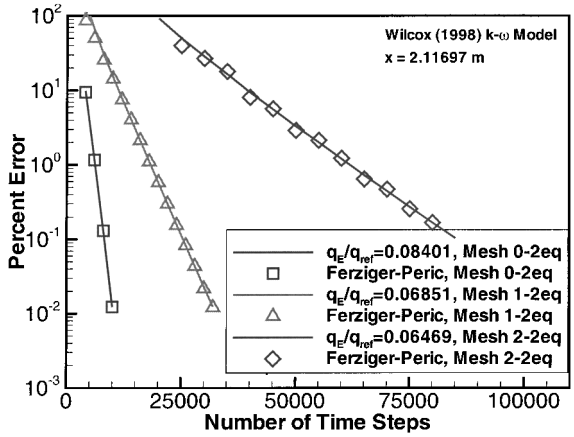

Fig. 10 Iterative convergence error of the surface heat flux for the Wilcox (1998) k–ω model at x = 2.11697 m with mesh 2eq.

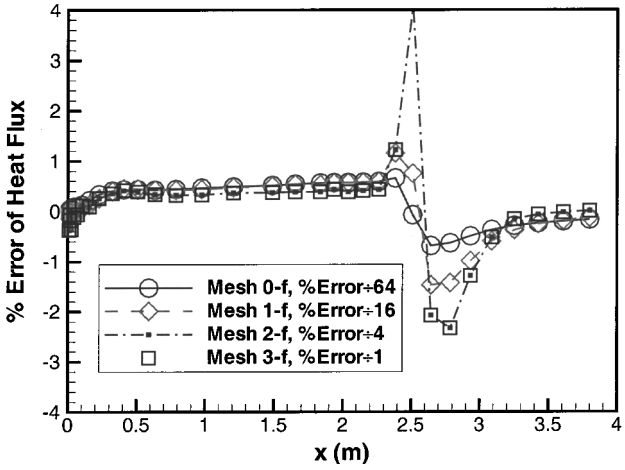

Fig. 11 Error in heat flux along the vehicle with mesh f refinement using the Spalart–Allmaras turbulence model.

If the mesh has been refined sufficiently where the solution error has second-order behavior (but not yet to the point where the first-order behavior occurs), then the errors on the four meshes have the following relationship:

$$\%\text{ error of } q_3 = (\%\text{ error of } q_2)/4 = (\%\text{ error of } q_1)/16$$

$$= (\%\text{ error of } q_0)/64 \tag{30}$$

In Eq. (30), the first equality will always be satisfied when Eq. (29) has been used. The other equalities will only be satisfied if the mesh has been sufficiently refined to be in the second-order asymptotic range. The normalized error of the wall heat flux along the vehicle is presented in Fig. 11. The laminar and turbulent flow regions are in the asymptotic range, while the transitional flow region is not in the asymptotic range. This result is not surprising because the mesh f grid does not use axial clustering at the transition region. The wall heat flux prediction in the laminar and fully turbulent regions have fine grid errors (mesh 3-f) of less than 0.5%, whereas the errors on mesh 2-f are less than 2%. Only the solutions on meshes 2-f and 3-f are considered sufficiently accurate for comparison with the flight measurements. The Richardson Extrapolated results could alternatively be used to provide more accurate numerical predictions than the finest mesh.

Spatial convergence has also been examined for the two-equation turbulence models using three mesh levels. The spatial error of the heat flux is given in Figs. 12–14 for the low-Reynolds-number k–ε, the Menter k–ω, and the Wilcox (1998) k–ω models, respectively. The spatial error in the laminar regions is under 2%, whereas in the transitional and turbulent regions the errors are under 5%. The results for both k–ω models indicate that the heat flux does not show a fully second-order grid convergence behavior, even in the fully turbulent region. The spike in the error for the two-equation models is due to movement of the transition location on the different size meshes and is more dramatic for the two-equation models due to the fine axial spacing around the transition point.

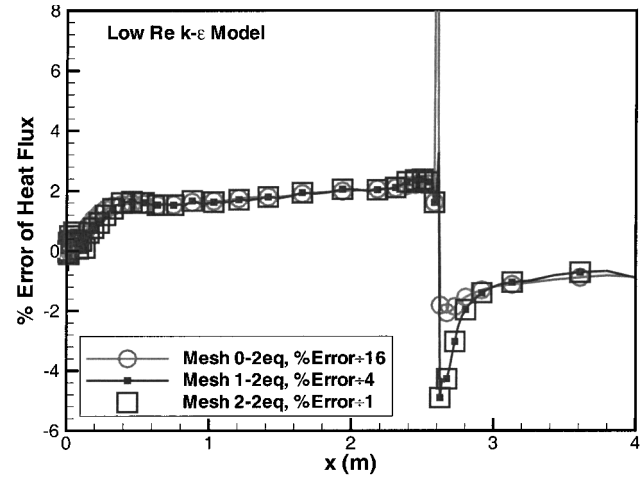

Fig. 12 Error in heat flux along the vehicle with mesh 2eq refinement using the low-Reynolds-number k–ε model.

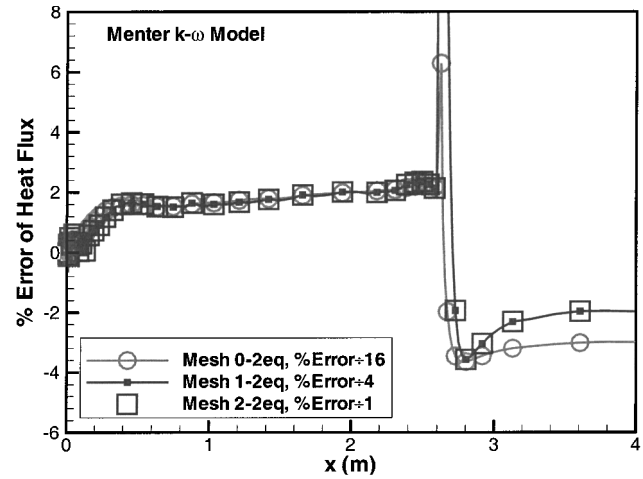

Fig. 13 Error in heat flux along the vehicle with mesh 2eq refinement using the Menter k–ω model.

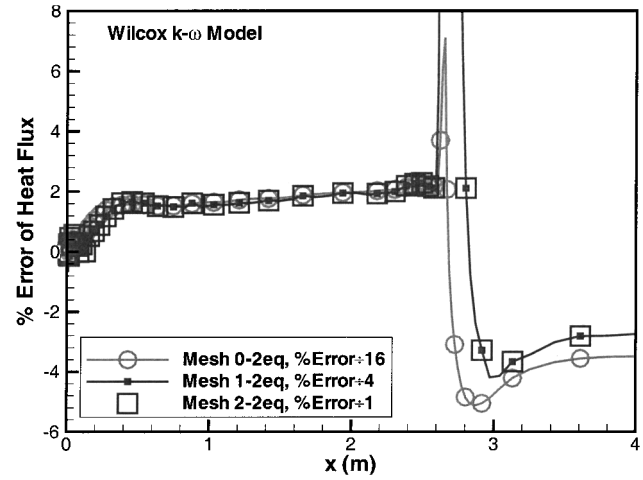

Fig. 14 Error in heat flux along the vehicle with mesh 2eq refinement using the Wilcox (1998) k–ω model.

Wall Heat Flux

The predictions of the wall heat flux on the Reentry F vehicle at an altitude of 24.4 km with the one-equation turbulence models are

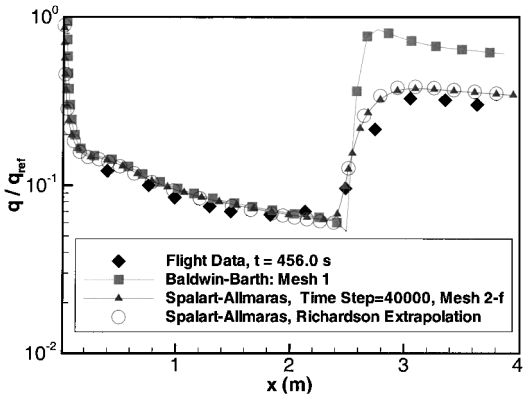

Fig. 15 Comparison of flight data for wall heat flux along Reentry F vehicle at an altitude of 24.4 km with predictions of the one-equation turbulence models.

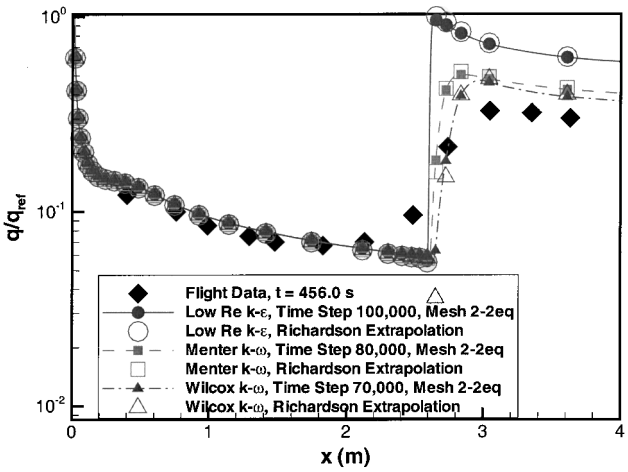

Fig. 16 Comparison of flight data for wall heat flux along Reentry F vehicle at an altitude of 24.4 km with predictions of the two-equation turbulence models.

given in Fig. 15 along with the flight data. The Spalart–Allmaras prediction uses the numerical solution with mesh 2-f and the Richardson Extrapolation results for this case. The Navier–Stokes results overpredict the laminar wall heat flux by roughly 10%. The Spalart–Allmaras model overpredicts the turbulent wall heat flux by approximately 15%. At this altitude, the vehicle has a 0.14-deg angle of attack, and the heat transfer measurements were made on the leeward side of the conical body. One would expect that a full three-dimensional solution, with the vehicle at angle of attack, would bring the prediction and flight data into closer agreement. The prediction with mesh 2-f is believed to be a sufficiently accurate steady-state solution that it can be used to validate the turbulence model, but there is some uncertainty in these results due to uncertainties in the freestream conditions and the flight measurements as discussed earlier.

The simulation with the Baldwin–Barth turbulence model (also shown in Fig. 15) overpredicts the laminar wall heat flux by roughly 10% and is in agreement with the simulation with the Spalart–Allmaras model. Of course, in the laminar flow region, the turbulence models should have no impact on the flow solution. The turbulent wall heat flux is overpredicted by roughly 100% with the Baldwin–Barth turbulence model. It is recommended that the Spalart–Allmaras model should be used rather than the Baldwin–Barth turbulence model for reentry flows.

Results with the Nagano and Hishida k–ε, the Menter k–ω, and the Wilcox (1998) k–ω models are presented in Fig. 16. Fine grid results with mesh 2eq are shown along with the results from Richardson Extrapolation. Again, the surface heat flux is overpredicted by approximately 10% in the laminar region for all of the simulations. The k–ε results show an overprediction of the turbulent heating rates by approximately 100%, possibly due to the use of the incompressible form of the turbulent kinetic energy production term. The two k–ω models show better agreement with the flight data, with the Menter model within 40% and the Wilcox (1998) model within 30% of the data. All three models display a peak in the turbulent heating just downstream of the specified transition plane, which is possibly due to crude behavior of the step transition method.

Conclusions

For the Mach 8 flat plate boundary layer flow with the step transition method, the Baldwin–Barth and both k–ω models gave transition at the specified location. The Spalart–Allmaras (with $f_{t1} = 0$ and f_{t2} included) and low-Reynolds-number k–ε models required an increase in the freestream turbulence levels to give transition at the desired location. All models predicted the correct skin-friction levels in both the laminar and turbulent flow regions.

For Mach 8 flat plate case, the transition location could not be controlled with the trip terms as given in the Spalart–Allmaras model. Several other approaches have been investigated to allow the specification of the transition location. The approach that appears most appropriate is to vary the coefficient that multiplies the turbulent production term in the governing partial differential equation for the eddy viscosity (method 2). When this coefficient is zero, the flow remains laminar. The coefficient is increased to its normal value over a specified distance to model the transition region crudely and obtain fully turbulent flow.

Predictions have been obtained for the Reentry F flight vehicle with both one- and two-equation turbulence models, where the transition location is specified a priori. Care has been taken to quantify the errors in surface heat flux distributions due to both iterative and grid convergence. The L_2 norms of the residuals exhibited oscillatory behavior after a three order of magnitude drop, thus requiring alternative methods for monitoring iterative convergence. An alternative method for iterative convergence error estimation was described. This method was used to reduce the iterative convergence errors below approximately 0.1% for all cases. Simulations were performed on three grid levels for the two-equation turbulence models and four grid levels for the Spalart–Allmaras model to assess the grid convergence errors. The errors in the laminar and turbulent regions were reduced to 2 and 5%, respectively, with the two-equation models and to below 0.5% for the Spalart–Allmaras model. Richardson Extrapolation was employed with the two finest grid solutions (assuming second-order spatial accuracy) to get even more accurate surface heat flux solutions.

For the Reentry F flight simulations, the axisymmetric turbulent predictions for wall heat flux with the Spalart–Allmaras, Menter k–ω, and Wilcox (1998) k–ω models are in reasonable agreement with the flight measurements. The wall heat flux in the turbulent region is overpredicted by 15% with the Spalart–Allmaras model, 30% with the Wilcox (1998) k–ω model, and 40% with the Menter k–ω model. These axisymmetric simulations assume the vehicle is at 0-deg angle of attack; thus, the agreement with the leeward-side data is expected to improve if three-dimensional simulations are performed at the reported 0.14-deg angle of attack. The Spalart–Allmaras model predictions for this case are much better than the results from the Baldwin–Barth model. The present form of the low-Reynolds-number k–ω two-equation model greatly overpredicts the heating in the fully turbulent region.

Acknowledgments

This work was supported by Sandia National Laboratories and the U.S. Department of Energy's Accelerated Strategic Computing Initiative. The authors would like to thank Basil Hassan and Kambiz Salari of Sandia National Laboratories for their helpful reviews of the manuscript.

References

[1] Masad, J. A., and Abid, R., "On Transition in Supersonic and Hypersonic Boundary Layers," *International Journal of Engineering Science*, Vol. 33, No. 13, 1995, pp. 1893–1919.

[2] Singer, B. A., "Modeling the Transitional Region," NASA CR 4492, Feb. 1993.

[3] Wilcox, D. C., *Turbulence Modeling for CFD*, 2nd ed., DCW Industries, La Canada, CA, 1998, Chap. 5, pp. 119–122 and 227–271.

[4]Huang, P. G., Bradshaw, P., and Coakley, T. J., "Turbulence Models for Compressible Boundary-Layers," *AIAA Journal*, Vol. 32, No. 4, 1994, pp. 735–740.

[5]Van Driest, E. R., "Investigation of Laminar Boundary Layer in Compressible Fluids Using the Crocco Method," NACA TN-2597, Jan. 1952.

[6]Van Driest, E. R., "Problem of Aerodynamic Heating," *Aeronautical Engineering Review*, Vol. 15, No. 10, 1956, pp. 26–41.

[7]Wright, R. L., and Zoby, E. V., "Flight Boundary-Layer Transition Measurements on Slender Cone at Mach 20," AIAA Paper 77-719, June 1977.

[8]Sutton, K., Zoby, E. V., and Hamilton, H. H., "Overview of CFD Methods and Comparison with Flight Aerothermal Data," *Symposium on Validation of Computational Fluid Dynamics*, CP-437, Vol. 2, AGARD, 1988, p. 16.

[9]Thompson, R. A., Zoby, E. V., Wurster, K. E., and Gnoffo, P. A., "Aerothermodynamic Study of Slender Conical Vehicles," *Journal of Thermophysics and Heat Transfer*, Vol. 3, No. 4, 1989, pp. 361–367.

[10]Wurster, K. E., Zoby, E. V., and Thompson, R. A., "Flow and Vehicle Parameter Influence on Results of Engineering Aerothermal Methods," *Journal of Spacecraft and Rockets*, Vol. 28, No. 1, 1991, pp. 16–22.

[11]Spalart, P. R., and Allmaras, S. R., "A One-Equation Turbulence Model for Aerodynamic Flows," AIAA Paper 92-0439, Jan. 1992.

[12]Spalart, P. R., and Allmaras, S. R., "A One-Equation Turbulence Model for Aerodynamic Flows," *La Recherche Aerospatiale*, No. 1, 1994, pp. 5–21.

[13]Wong, C. C., Blottner, F. G., Payne, J. L., and Soetrisno, M., "Implementation of a Parallel Algorithm for Thermo-Chemical Nonequilibrium Flow Solutions," AIAA Paper 95-0152, Jan. 1995.

[14]Wong, C. C., Soetrisno, M., Blottner, F. G., Imlay, S. T., and Payne, J. L., "PINCA: A Scalable Parallel Program for Compressible Gas Dynamics with Nonequilibrium Chemistry," Sandia National Labs., Rept. SAND 94-2436, Albuquerque, NM, April 1995.

[15]Hassan, B., Kuntz, D. W., and Potter, D. L., "Coupled Fluid/Thermal Prediction of Ablating Hypersonic Vehicles," AIAA Paper 98-0168, Jan. 1998.

[16]Kuntz, D. W., Hassan, B., and Potter, D. L., "An Iterative Approach for Coupling Fluid/Thermal Predictions of Ablating Hypersonic Vehicles," AIAA Paper 99-3460, June 1999.

[17]Baldwin, B. S., and Barth, T. J., "A One-Equation Transport Model for High Reynolds Number Wall-Bounded Flows," NASA TM-102847, Aug. 1990.

[18]Menter, F. R., "Eddy Viscosity Transport Equations and Their Relation to the k–ε Model," *Journal of Fluids Engineering*, Vol. 119, No. 4, 1997, pp. 876–884.

[19]Nagano, Y., and Hishida, M., "Improved Form of the k–ε Model for Wall Turbulent Shear Flows," *Journal of Fluids Engineering*, Vol. 109, No. 2, 1987, pp 156–160.

[20]Menter, F. R., "Two-Equation Eddy-Viscosity Turbulence Models for Engineering Applications," *AIAA Journal*, Vol. 32, No. 8, 1994, pp. 1598–1605.

[21]Squire, L. C., "The Accuracy of Flat Plate, Turbulent Skin Friction at Supersonic Speeds," *Aeronautical Journal*, Vol. 104, No. 1036, 2000, pp. 257–263.

[22]Menter, F. R., Grotjans, H., and Unger, F., "Numerical Aspects of Turbulence Modeling for the Reynolds Averaged Navier–Stokes Equations," *Computational Fluid Dynamics Lecture Series 1997-02*, von Kármán Inst. for Fluid Dynamics, Rhode Saint Genese, Belgium, 1997, pp. 1–45.

[23]Launder, B. E., and Sharma, B. E., "Application of the Energy Dissipation Model of Turbulence to the Calculation of Flow Near a Spinning Disc," *Letters in Heat and Mass Transfer*, Vol. 1, No. 2, 1974, pp. 131–138.

[24]Theodoridis, G., Prinos, P., and Goulas, A., "Test Case T3—Free Stream Turbulence," *Numerical Simulation of Unsteady Flows and Transition to Turbulence*, edited by O. Pironneau, W. Rodi, I. L. Ryhming, A. M. Savill, and T. V. Truong, Cambridge Univ. Press, Cambridge, England, U.K., 1992, pp. 368–373.

[25]Wilcox, D. C., "Reassessment of the Scale Determining Equation for Advanced Turbulence Models," *AIAA Journal*, Vol. 26, No. 11, 1988, pp. 1299–1310.

[26]*US Standard Atmosphere*, National Oceanic and Atmospheric Administration, NASA, and U.S. Air Force, Washington, DC, Oct. 1976.

[27]Roberts, G. O., "Computational Meshes for Boundary Layer Problems," *Proceedings of the Second International Conference on Numerical Methods in Fluid Dynamics*, edited by M. Holt, Vol. 8, Lecture Notes in Physics, Springer–Verlag, New York, 1971, pp. 171–177.

[28]Tannehill, J. C., Anderson, D. A., and Pletcher, R. H., *Computational Fluid Mechanics and Heat Transfer*, 2nd ed., Taylor and Francis, Bristol, PA, 1997, p. 335.

[29]Ferziger, J. H., and Peric, M., *Computational Methods for Fluid Dynamics*, 1st ed., Springer–Verlag, Berlin, 1996, pp. 115–126.

[30]Ferziger, J. H., and Peric, M., "Further Discussion of Numerical Errors in CFD," *International Journal for Numerical Methods in Fluids*, Vol. 23, No. 12, 1996, pp. 1263–1274.

[31]Roache, P., *Verification and Validation in Computational Science and Engineering*, 1st ed., Hermosa, Albuquerque, NM, 1998, p. 109.

[32]Carpenter, M. H., and Casper, J. H., "Accuracy of Shock Capturing in Two Spatial Dimensions," *AIAA Journal*, Vol. 37, No. 9, 1999, pp. 1072–1079.

[33]Roy, C. J., McWherter–Payne, M. A., and Oberkampf, W. L., "Verification and Validation for Laminar Hypersonic Flowfields," AIAA Paper 2000-2500, June 2000.

T. C. Lin
Associate Editor